

PPD Summer Placement Report

Glass-GEM Simulations for the MIGDAL Experiment

Ruize Li*

University of Cambridge
Cambridge, UK

ABSTRACT

The Migdal effect, effect of additional ionization or excitation during a nuclear recoil, is widely used in direct detection of dark matter particles, particularly those with lower masses. The Migdal in Galactic Dark mAtter expLoration (MIGDAL) experiment aims to directly observe and measure, for the first time, the Migdal effect. The detector operates with an optical Time Projection Chamber with fiducial volume $8\text{ cm} \times 8\text{ cm} \times 3\text{ cm}$, filled with low-pressure CF_4 . Both optical and electrical readout rely highly on the performance of the stack of glass-Gas Electron Multipliers (GEMs), where signal amplification takes place. In this report, I will discuss the modelling of the GEMs in COMSOL and simulation with the Garfield++ package, leading to optimisation of the glass-GEMs used in the MIGDAL experiment.

*r1737@cam.ac.uk

Contents

1	Introduction	1
2	Detector Set-Up	2
2.1	Neutron source at NILE	3
2.2	Optical time projection chamber	3
3	Properties of CF₄	6
3.1	Electron transport properties: simulation using Magboltz	6
3.2	Scintillation and light production	7
4	Single GEM Simulations	7
4.1	Charge production	7
4.2	Electric field corrections	9
4.3	Light production	10
4.4	Trapezoid holes	11
5	Double and Triple GEM Simulations	11
5.1	Multi-stage simulation	12
5.2	Gain and charge distribution on ITO	14
5.3	Light collection map	15
6	Discussion and Conclusion	19
A	Distribution at the bottom of transport region	22
B	Code for determining passage	23

1 Introduction

The direct search for Dark Matter (DM) typically looks for a kind of interaction called Nuclear Recoil (NR), where a DM particle scatters off a nuclei via weak interaction. However, this effect has a threshold, below which NR signal is not detectable [1]. The threshold depends on the mass of detecting medium. For experiments using Liquid Xenon (LXe) [2, 3, 4] or germanium [5] it is usually $\mathcal{O}(10\text{ GeV})$, while mediums such as CF₄, helium and silicon provides a lower threshold

at sub-GeV level [6]. DM candidates possible for direct search are mainly Weakly Interacting Massive Particles (WIMPs) [7], axions [8] and axion-like particles [9], whose mass ranges from 10^{-15} eV to 10^9 eV, indicating that a way of detecting lower-mass DM particles is needed.

In 1941 A. Migdal proposed an effect, that there is a possibility for ionisation during an NR, giving out an extra electron [10]. This electron should come from the same position of the NR, and could be detected as an Electric Recoil (ER) in current experiments [11]. Up to now, this effect is widely used in DM direct search [12]. In these experiments, neutron acts as a perfect proxy to calibrate NR response and the associated Migdal electron emission. Although there are theoretical calculations and experiments investigating this effect [13, 14, 15], it has never been directly observed and measured. The MIGDAL experiment [16] was established to achieve the unambiguous detection of the Migdal effect using an optical Time Projection Chamber (TPC), where a direct image of the effect and fine reconstruction of both energy and position are made possible. Plus, the Migdal electron favours the opposite direction of NR track [13], which provide more possibility of direct imaging.

In the MIGDAL TPC, electrons from ionisation are collected by a stack of glass-Gas Electron Multipliers (GEMs). GEM was invented by F. Sauli in 1997 [17], it typically has etched holes of diameter $\sim 70\text{ }\mu\text{m}$ and pitch $\sim 100\text{ }\mu\text{m}$. However, this geometry is not suitable for the MIGDAL experiment. As we will see in later sections, the mean free path of electrons in such a low pressure (50 Torr) is impossible for reliably developing electron avalanches. On the other hand, to image a Migdal event, the MIGDAL experiment rely on GEMs to produce not only electrical, but also optical signal from electron avalanches in the GEM holes, requiring high transparency of GEMs. Luckily, GEM detectors have greatly developed over the past ~ 30 years, leading to different types using different materials, shapes and sizes, and has been used in a variety of experiments. Classical GEMs are used in the CMS experiment [18], while Thick-GEMs (THGEMs) are widely used in TPC experiments [19, 20, 21]. Glass-GEM is a special kind of THGEM made from a glass substrate with copper-clad [22], which was chosen for the MIGDAL experiment because it allows better light transmission, at the same time gives more space for avalanches.

While the choice of glass-GEMs with larger holes and pitch addresses the challenges of low-pressure operation and optical readout, achieving optimal signal amplification and light collection requires careful tuning of the GEM geometry and operating conditions. In this report, we discuss the modelling and simulation of the GEMs using the multi-physics software COMSOL and the Garfield++ package. In the following section we introduce the detector set-up. Section 3 reviews the properties of pure CF_4 as the medium. Section 4 and 5 reports the simulation and optimisation of single-GEM and multi-GEM systems, respectively. Finally, we discuss our results and conclude the report in the last section.

2 Detector Set-Up

The MIGDAL experiment is based in the Rutherford Appleton Laboratory (RAL), using D-D and D-T neutron generator beams at the NILE facility. As shown in Fig. 1, the experiment is entirely shielded by lead and concrete when in operation. The long copper collimator limits the incoming angle of neutrons, acts as an energy filter, and controls background from surrounding materials as well.

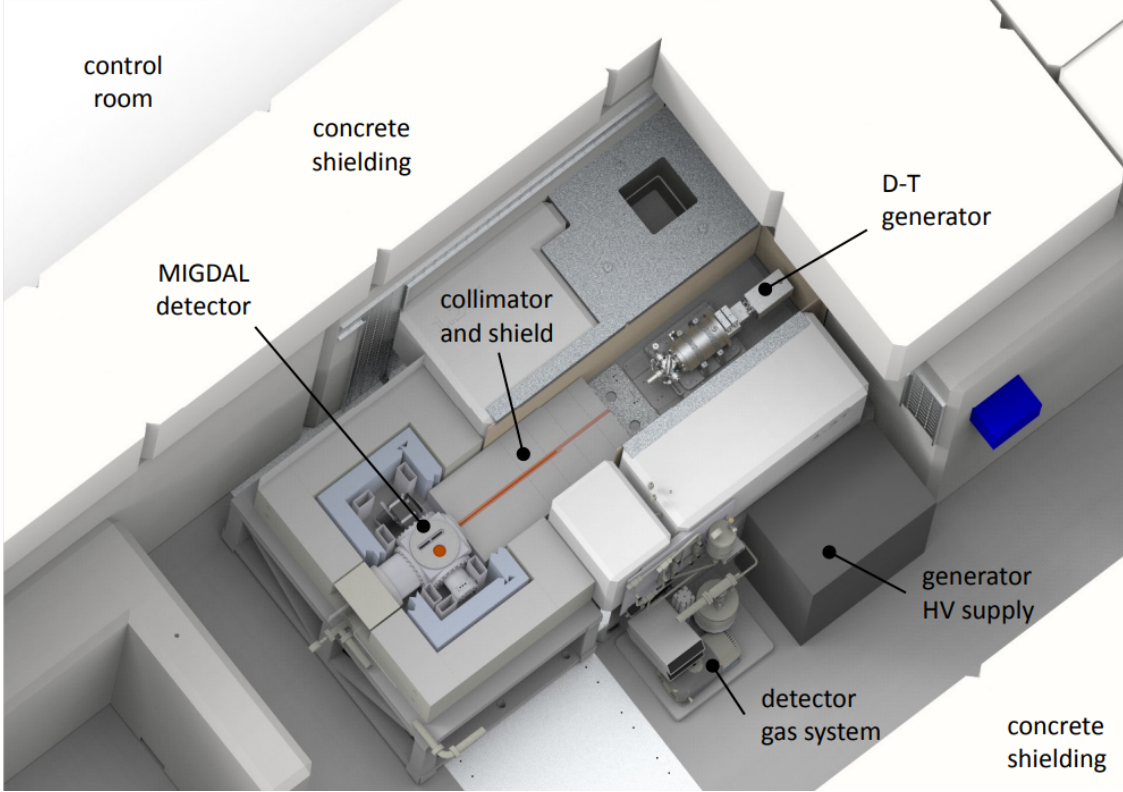


Figure 1: MIGDAL experiment viewed from top [16], using D-T neutron generator as an example, the collimator for D-D neutron is just under half the length. High Voltage (HV) supply and Data AcQuisition (DAQ) system are CAEN products.

2.1 Neutron source at NILE

The D-D neutron generator at NILE produces neutrons with mean energy 2.45 MeV in lab frame, though the actual spectrum is slightly broadened due to kinematic effects and target thickness. Since it gives low-energy events, this type of neutron generators is widely used in LXe TPC experiments searching for dark matter [23, 24, 25]. The D-T neutron generator provides neutrons of higher energy, typically 14.1 MeV in lab frame. Due to the higher neutron energy, D-T generators can induce more energetic NR signal and are valuable for calibrations that require probing the response of detectors in the high-energy region. With both generators, it is possible to perform systematic studies of NR and the associated Migdal electron emission over a wide recoil energy range, and enabling cross-checks of detector performance and background rejection under different neutron-scattering regimes.

2.2 Optical time projection chamber

The electric field in the drift region (200 V cm^{-1}) is designed to minimise *transverse* diffusion. Note that even for a 3 cm gap, we still need a few copper field-shaping rings. Field in the transport region (between GEMs) is set to 600 V cm^{-1} compensating between diffusion and drift velocity. As for the induction region (below the last GEM), a strong, sharp signal at ITO is preferred, so

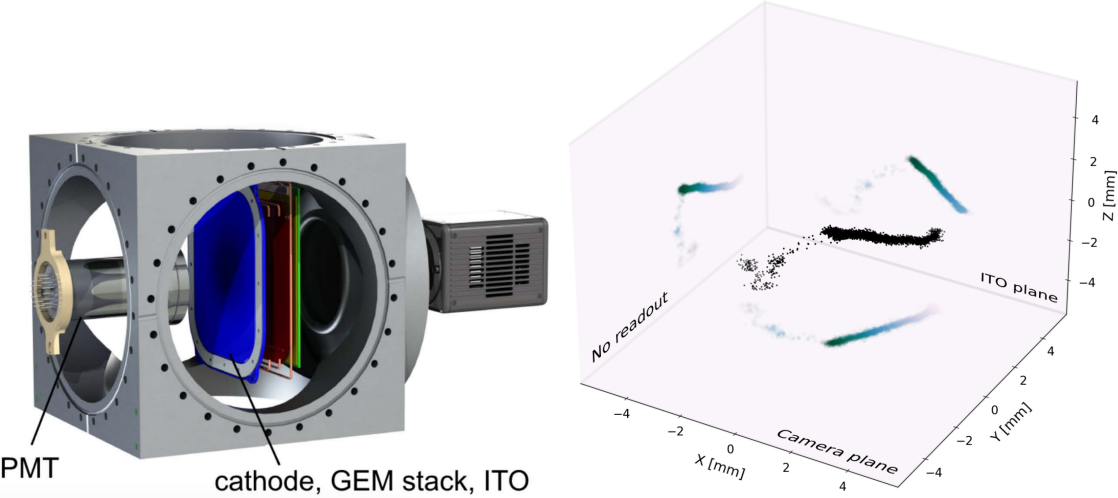


Figure 2: Left: A detailed structure of the optical TPC for MIGDAL experiment [16]. The GEM stack and ITO mesh are placed vertically, with the camera on the same side. A PhotoMultiplier Tube (PMT) is placed on the other side, collecting scintillation light and acting as an external trigger. In the future the PMT will probably be replaced by an array of four PMTs, each with effective area $48.5 \text{ mm} \times 48.5 \text{ mm}$, contributing to position reconstruction. Right: An expected "Migdal-like" event [16]. Readouts from qCMOS and ITO are indicated.

the induction field is set to 400 V cm^{-1} to minimise *longitudinal* diffusion. These data are from simulations using the Magboltz package, as shown in Fig. 3.

A Vacuum UltraViolet (VUV) sensitive Hamamatsu R11410 PMT is mounted opposite the quantitative CMOS (qCMOS) camera and used as part of the optical readout system to detect both the primary scintillation light (S1) generated promptly in the CF_4 gas by the initial particle interaction, and the secondary scintillation light (S2) produced in the GEM holes during electron avalanche. The S1 signal provides the interaction start time, enabling reconstruction of the absolute depth (z -coordinate) of the event, while the larger S2 pulse serves as the *external trigger* for the DAQ and allows cross-checking of energy deposition. The high sensitivity of the PMT to both VUV and visible components of CF_4 scintillation, combined with its low dark count rate, enables a NR detection threshold down to $\sim 50 \text{ keV}$ for central events. With upgraded PMTs, the timing can be accurate to several nanoseconds, which gives a spatial precision about a millimetre not only along the z -direction, but also in the x - y plane.

The glass-GEM stack — component we hope to optimise — has two (or three) layers of GEMs, leaving a 2 mm transport gap between each other. The active measuring region of the GEM stack is $10 \text{ cm} \times 10 \text{ cm}$, fully covering the fiducial region. Each GEM is $570 \mu\text{m}$ thick with $2 \mu\text{m}$ copper plate at top and bottom. The holes are cylindrical, hexagonal close packed with pitch $280 \mu\text{m}$. We vary several parameters and observe the change to the overall gain and light collection of glass-GEM. The parameters are listed below.

- Diameter of the hole: from $150 \mu\text{m}$ to $250 \mu\text{m}$. We will also observe the effect of etched rims on gain and collection efficiency.
- Voltage across the GEM: from 510 V to 600 V , only for two diameters we are using, $170 \mu\text{m}$ and $210 \mu\text{m}$.

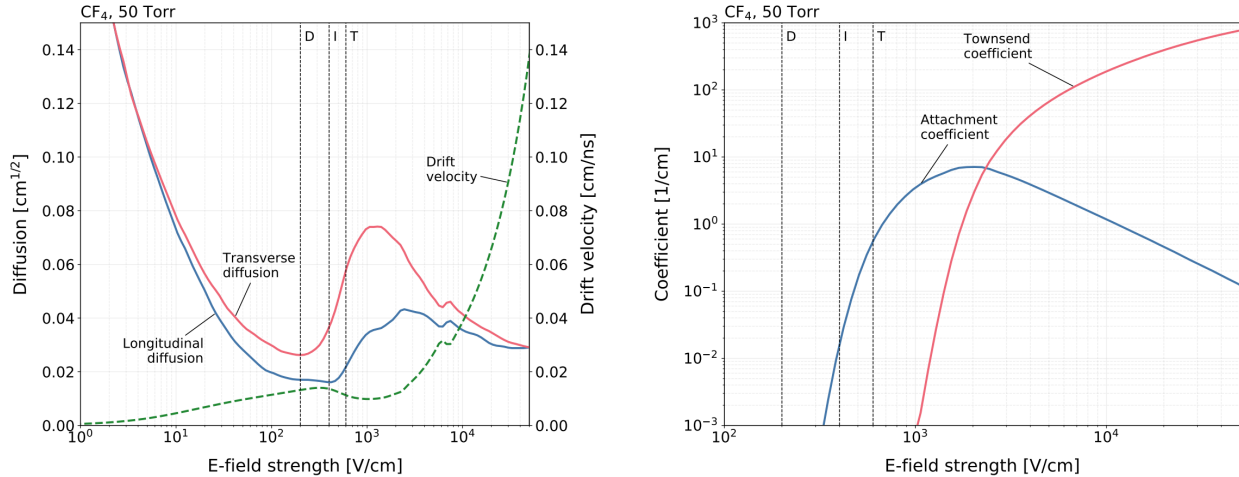


Figure 3: Left: Electron transport properties of CF₄ at 50 Torr for different electric fields. Right: Attachment and Townsend coefficients as a function of electric field. Plots are generated by the collaboration [16].

- Shape of the hole: using a simple model of parallel plates.
- Alignment of multiple glass-GEMs: AAA (all aligned) or ABA (misaligned, middle layer shifted by half a pitch).

The ITO anode plate plays a dual role as the final charge collection stage and as a transparent optical window for the qCMOS camera. Fabricated from a low-resistivity ($4 \Omega/\text{sq}$) ITO film deposited on a 1.1 mm thick glass substrate, it is patterned into 120 parallel strips with a pitch of 833 μm . This segmentation reduces the capacitance per readout channel, lowering electronic noise and improving timing precision, while providing lateral coordinate information to complement the drift-time measurement from the PMT. The optical transparency of the ITO layer allows the secondary scintillation light from the final GEM to pass through with minimal attenuation, enabling the camera to image particle tracks without (too much) obstruction. The qCMOS camera is focused on the bottom surface of the last GEM at the distance of $\sim 12 \text{ cm}$ [16].

The performance of GEMs makes a huge difference on almost *every* source of readout from our detector. First, GEMs directly influence PMT measurements by determining the size and time structure of S2. Higher GEM gain boosts the light yield, improving signal-to-noise ratio, but excessive gain can increase afterpulse or space charge effects, impacting timing resolution. Second, GEMs influence ITO readout directly by controlling the overall gain and spatial distribution of electrons. Well-tuned GEM gain yields both strong and sharp pulses that are easy to distinguish from noise, whereas gain instabilities can degrade both resolution and event reconstruction reliability. Finally, different geometries of GEMs lead to different transparency and light collection efficiency at the qCMOS camera. A higher gain means more photons are produced, while a larger GEM hole diameter will increase the probability for a photon to be collected.

Overall, the arbitrariness of the selection of GEM-related parameters indicates great potential, and suggests that it is the key towards the optimisation of instrumentation for the MIGDAL experiment. Before going into details, we need to investigate first how electrons move within, and interact with the detector and the medium.

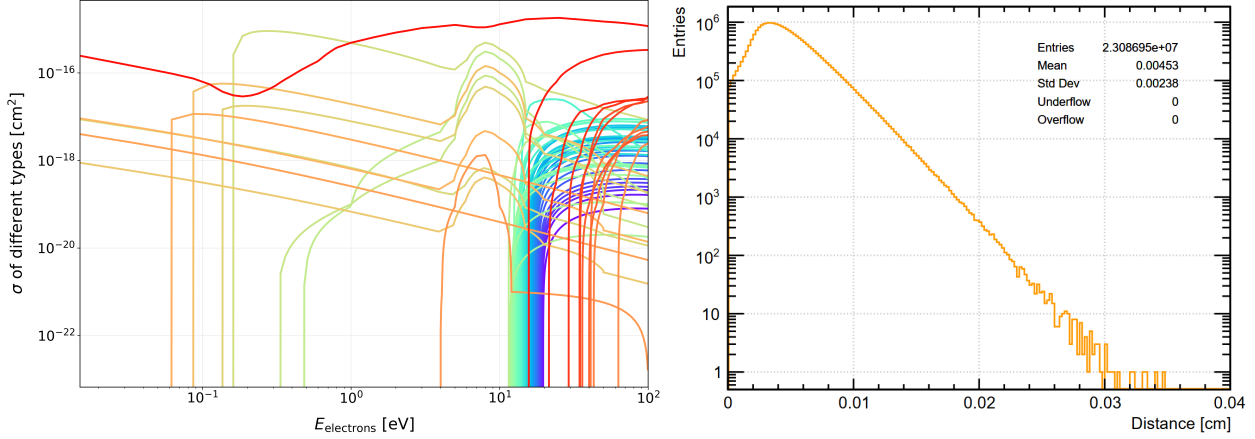


Figure 4: Left: Electron cross section of various types of interactions, from red to purple: elastic collisions, ionisations, attachment (starting at 4 eV), vibrational, and neutral dissociation. Right: MC simulation gives a 45.3 μm mean free path between *collisions* in a 9825 V cm^{-1} uniform electric field. Townsend coefficient related to this field is 186 cm^{-1} , corresponding to 53.8 μm mean free path between *ionisations*. If 30 % argon is added, the mean free path between *collisions* will reduce to 41.3 μm , leading to a significantly higher gain.

3 Properties of CF₄

In the MIGDAL experiment, CF₄ is selected as the base gas because it combines a high scintillation yield with an emission spectrum well matched to qCMOS sensitivity, enabling direct imaging. Its relatively low mass nuclei provide clear, trackable NRs with minimal multiple scattering, and its optical properties allow simultaneous PMT timing and imaging.

Adding a noble gas to the CF₄ can generally increase scintillation probabilities, common choices are helium, argon and xenon. Helium has very light nuclei, giving long recoil tracks but low ionization yield [26]. On the other hand, xenon is very heavy and has high ionization yield but produces short, dense tracks that are harder to image in low-pressure gas. Argon sits in between, offering a good balance of track length, ionization, and scintillation yield [27]. In the MIGDAL experiment, the addition of noble gas can be done through the gas system directly, and the CF₄-Ar mixture with 7 : 3 ratio performed stably. However, in this report we are not including details about gas mixtures, as the excitation and scintillation mechanisms are not well-understood.

3.1 Electron transport properties: simulation using Magboltz

Magboltz is a software package that enables calculation of electron transport parameters by simulating electron collisions with gas molecules over a wide range of electric and magnetic fields. As shown in Fig. 3, we carefully choose drift, induction and transport fields according to electron transport parameters in CF₄ at 50 Torr.

The electric field in a GEM hole, however, can be as high as $1 \times 10^5 \text{ V cm}^{-1}$ on central axis, and several times higher near the edge. Careful investigation is needed within this region. A GasFile was generated particularly for high-field, from which we can read any property of electrons. To check the validity of Magboltz result, we performed Monte Carlo (MC) simulation in a uniform field to check the (first) Townsend coefficient, α , as shown in Fig. 4.

From both Magboltz and MC simulations, we expect a $\sim 50 \mu\text{m}$ mean free path, using the approximation

$$\text{Mean free path} \simeq \frac{1}{\alpha}. \quad (1)$$

This indicates that larger GEM holes would make avalanches more fully developed, resulting in a higher gain. We then performed avalanche between a parallel plate with $570 \mu\text{m}$ separation and 9825 V cm^{-1} uniform field. The gain of a *full* avalanche, calculated using different methods, are shown in Table 1. Note that, a full avalanche could be as wide as $600 \mu\text{m}$ in diameter, several times the diameter of the hole. As a result, in our glass-GEM, there are always electrons hitting the glass wall and copper plate below. Having larger holes could potentially decrease the loss.

Table 1: Multiplication factor for a full avalanche between parallel plates.

Method	Gain	Comments	Reason
Runge-Kutta	31495	Overestimates	Ignoring attachments
$\exp \left[\int_A^B dx \alpha(x) \right]$	33389	Overestimates	Ignoring attachments
MC	21000	Underestimates	Early attachments

3.2 Scintillation and light production

Although Magboltz provides every information about electron transport, it does not include information about photon production. In fact, there's currently no way to physically simulate the process, the only thing we can do is to tune parameters to match the experimental data.

Scintillation of CF_4 in various field strengths and pressures were measured experimentally [28], giving a robust result of $N_\gamma/N_e = 34\%$ under all conditions, where N_γ is the number of photons produced, and N_e is the number of electrons produced. To simulate this, we took advice from T. Szwarcz² and chose ionisations with energy loss $\text{ELOSS} > 14 \text{ eV}$, before applying a scintillation probability of 33%. With these adjustments, the simulated data gives the same N_γ/N_e as the experiment, as shown in Fig. 9 (left).

With the basic knowledge of detector and medium above, we can move on and carry out simulations for the glass-GEMs.

4 Single GEM Simulations

Geometry and field map of a single GEM was generated using COMSOL, a multiphysics simulation software that uses Finite Element Method (FEM). As shown in Fig. 5, we only include a motif of the GEM, as Garfield++ is able to generate the whole volume using mirror symmetry w.r.t. both x - z and y - z planes. The contour lines of electric field *magnitude* are also shown in Fig. 5. It is clear that electric field takes maximum value along the top and bottom circular edge of the hole.

4.1 Charge production

We start the avalanche at the top-centre of the GEM hole. Later we will show that the distribution of starting points does not affect the gain and distribution at exit very much,

²Previous PPD summer student, more information on his [personal website](#).

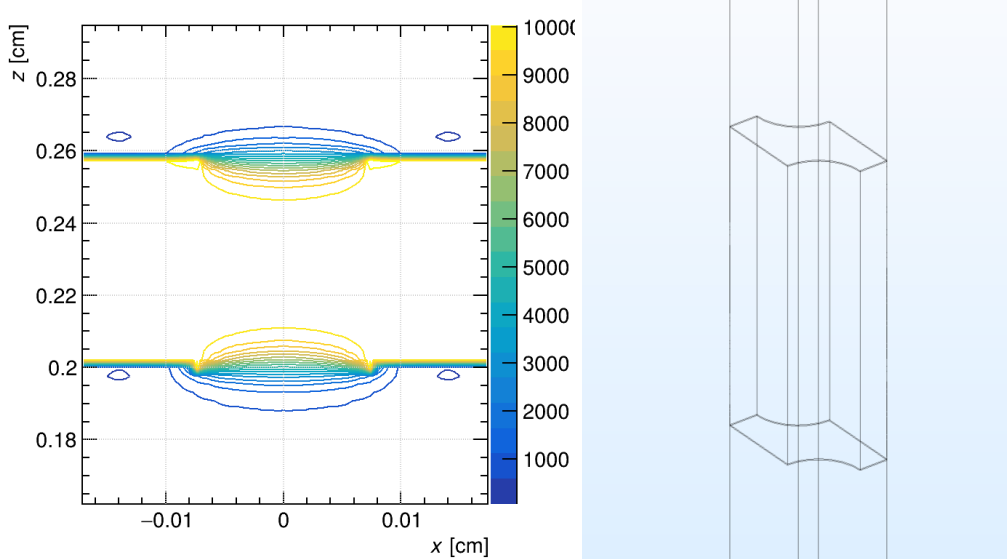


Figure 5: Left: $|\vec{E}|$ contours in a cross-section of GEM, through its axis. Right: Geometry of a single GEM from COMSOL, where we left 2 mm drift and induction gaps above and below, respectively.

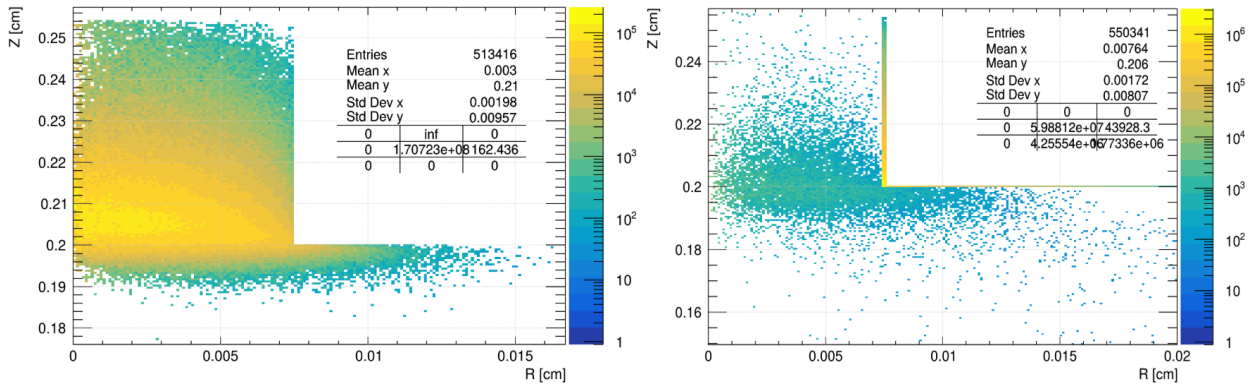


Figure 6: Two-dimensional distribution of start points (left, Startpoints) and end points (right, Endpoints) of electrons during avalanches (zoomed in).

as long as most electrons start reasonably away from the glass wall. Using the function `AvalancheMicroscopic::GetElectrons`, we are able to investigate the effect of non-uniform electric field on ionisations and attachments. Fig. 6 shows that the largest number of electrons were produced at the bottom-centre of the hole, while the largest number of electrons were lost on glass wall and bottom copper plate.

Note that, although the absolute number for different kinds of endpoints vary a lot, the proportions vary only slightly. About 79 % electrons were lost on the glass wall and copper plate, which brought us concerns on the stability of GEMs with large holes, which will be discussed later in Section 6.

Careful treatment of the gain is needed, since electrons can end by attachment, hitting somewhere, or leaving the defined sensor region. Each electron endpoint is denoted using a status code, which indicates how the track ends. Therefore, we use both *position* and *status* conditions. Only when the

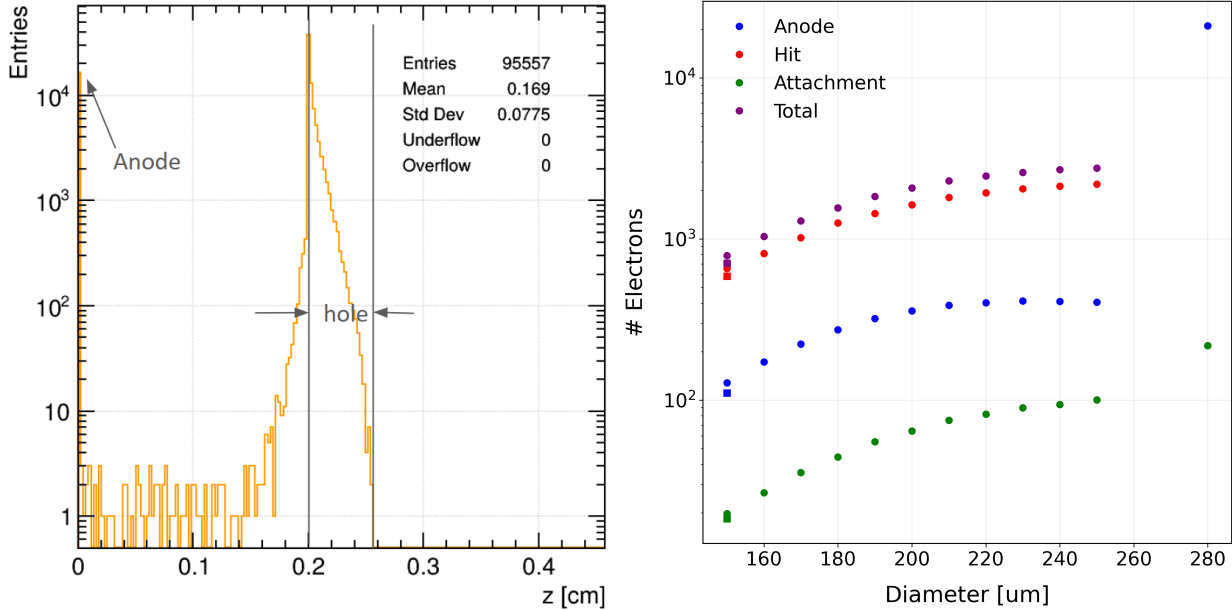


Figure 7: Left: Distribution of z -coordinate of electron Endpoints, using result from $210\text{ }\mu\text{m}$ as an example. Right: Gain, as a function of diameter. The points at $280\text{ }\mu\text{m}$ correspond to the parallel plate with a full avalanche. The squares at $150\text{ }\mu\text{m}$ are GEM with $10\text{ }\mu\text{m}$ rim at the bottom copper plate.

endpoint of an electron is within a certain coordinate range and meets the right status, it is judged to have reached the anode.

As shown in Fig. 7, the gain saturates at $230\text{ }\mu\text{m}$, and slowly decrease afterwards due to smaller field strength and larger proportion of attachments. Surprisingly, glass-GEM with a $10\text{ }\mu\text{m}$ rim [20] didn't perform better compared to that without. This is probably because of increased tip effect after adding the rim. However, due to limitations in manufacturing technology, the rim's cross-section deviates significantly from a perfect rectangle [29]. As most electrons are stopping at the corner, and a small difference in geometry will lead to significant difference in electric field, we did not investigate the effect of rims further.

4.2 Electric field corrections

In Section 2, we stated that electric fields in drift, induction and transport regions are designed specifically for some purposes. However, when varying diameter of the GEM holes, we have changed the boundary conditions of electric field, so it changes in these regions as well. The "leakage" of field strength from GEM holes to outside can be compensated by changing voltages of various planes, and will be used in Section 5 to minimise diffusion. Here, we compare the voltage dependence of two diameters used in the MIGDAL detector, $170\text{ }\mu\text{m}$ and $210\text{ }\mu\text{m}$, as shown in Fig. 8

The gain was fitted using an exponential model,

$$G = A \exp(Bx + C), \quad (2)$$

where A , B and C are constant parameters for each geometry. Our simulated results matches the model well [30].

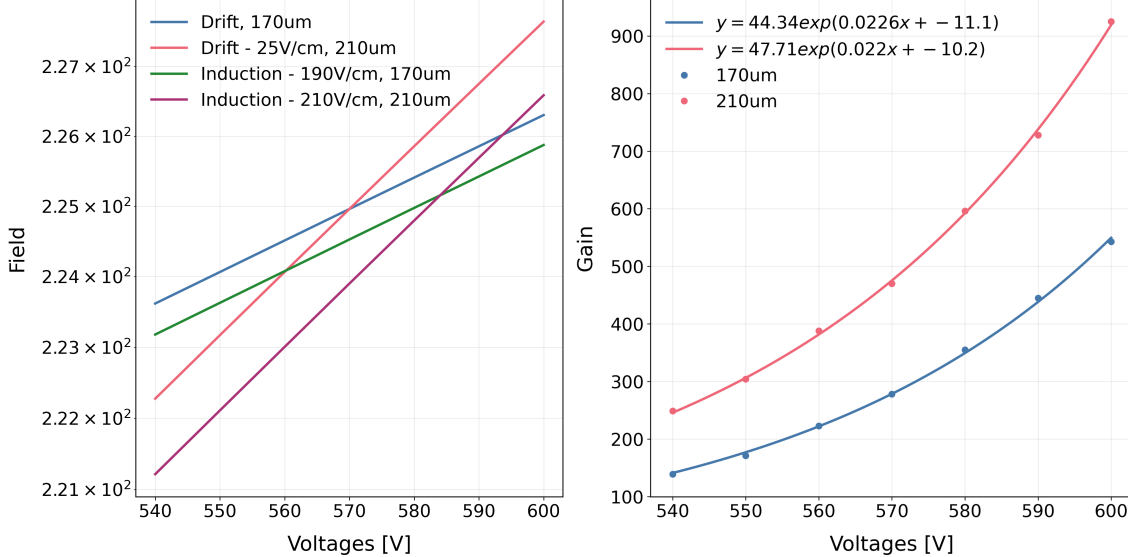


Figure 8: Left: Field strengths in the drift and induction regions for 170 μm and 210 μm glass-GEMs, in the single-GEM setup. Right: Gain as function of voltage across the GEM.

Although the gain varies as a simple exponential, there are many differences in the electric fields. First, electric field along the central axis experiences a "leakage", as mentioned before. The "leakage" is linear in logarithm scale for all three regions, providing quantitative instruction on voltage corrections. However, at positions closer to the glass wall, the "leakage" is smaller, leading to a non-uniform radial distribution for large holes. Along a line parallel to the z -axis closer to the glass wall, we could see the abrupt change in electric field. GEM with a larger radius has a larger change, for the 250 μm GEM, the electric field can rise to $3 \times 10^4 \text{ V cm}^{-1}$ and drop down in only $\sim 50 \mu\text{m}$.

This reminds us a limitation of FEM. The expected free path can be expressed as

$$\langle l \rangle = \int_0^\infty ds \exp \left[- \int_0^s ds' \alpha(E(\vec{x}')) \right], \quad (3)$$

where α is the first Townsend coefficient, as a function of electric field. It's easy to check that when E is constant, the integral gives $1/\alpha$. When electric field changes abruptly, the integral done by FEM would introduce significant errors. Notably, such region also corresponds to the most electron production and attachment processes. As a result, it is challenging to produce reliable result on the effect of rims using Garfield++.

4.3 Light production

Based on the studies of scintillation mechanism discussed before, we make some further assumptions:

- Photon is produced at the same position as ionisation.
- Photon is emitted to a random direction.

Using a `UserHandle` function, we can access the positions, energy loss and other information of the interaction. Plus, we are free to customise the function, determine whether the photon is able

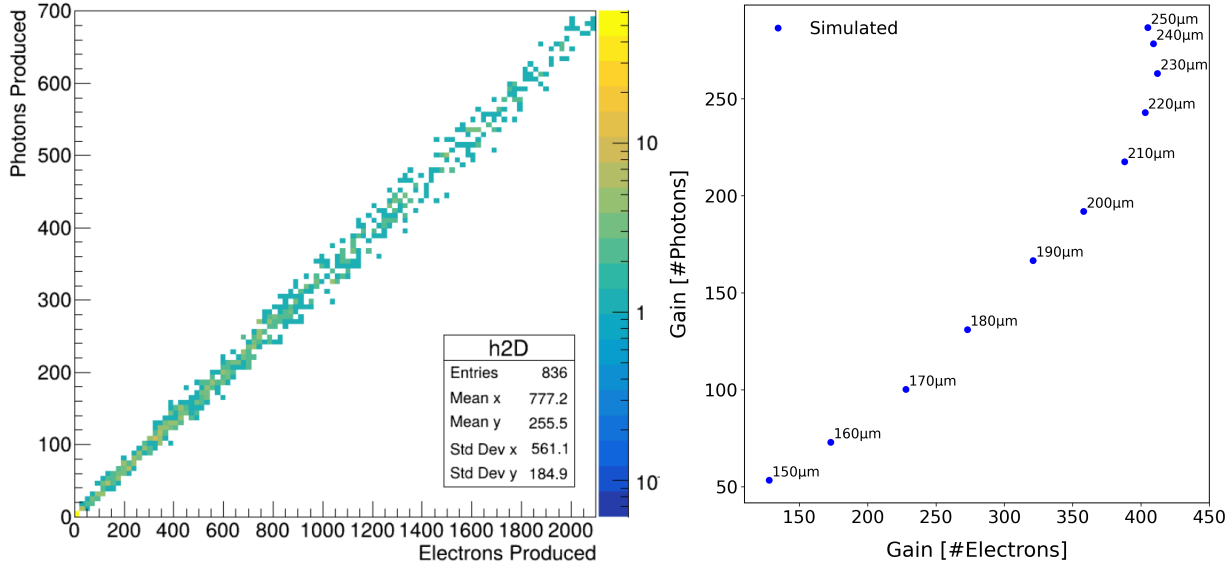


Figure 9: Left: N_γ as a function of N_e , linearity is robust against change in both electric field and gas pressure. Right: Number of photons against number of electrons reaching the anode per avalanche, at different voltages across GEM.

to reach the anode, and where it ends. Note that, we are not considering photons reflecting and refracting between the copper plates, which leads to a wider position distribution at the anode plane.

We compared the gain of photons per avalanche and that of electrons in Fig. 9 (right). There's a clear sign of saturation, however not observed up to 250 μm , which corresponds to somewhere before a "fully open" structure³. Comparison between 170 μm and 210 μm GEMs shows a increase in the standard deviation of x and y from 0.95 mm to 1 mm ($\Delta \simeq 0.18 \cdot \text{pitch}$), which is relatively small. Increasing GEM diameter can increase the gain of photons approximately linearly, with little effect on the position resolution.

4.4 Trapezoid holes

Etching the glass-GEM plate from only one side, it is possible to produce trapezoid-shape holes with a larger diameter below. However, it is very hard to keep electric field uniform within the induction region, and the fieldlines pointing sideways further broadens transverse distribution. Also, as most photons and electrons are produced at the lower-half of GEM hole, decrease in electric field would affect light production significantly. To summarise, incorporating GEMs with trapezoid-shaped holes is not a suitable choice for our detector.

5 Double and Triple GEM Simulations

In the MIGDAL experiment, we use a stack of two or three glass-GEMs to increase the gain, while keeping stable performance of the detector. In order to investigate the two-dimensional position resolution and the quality of imaging, it would be helpful to simulate the behaviour of two or three GEMs. However, a full avalanche for three GEMs takes more than ten hours to develop,

³As a fully open structure will not have regions with high electric fields, saturation must happen before that.

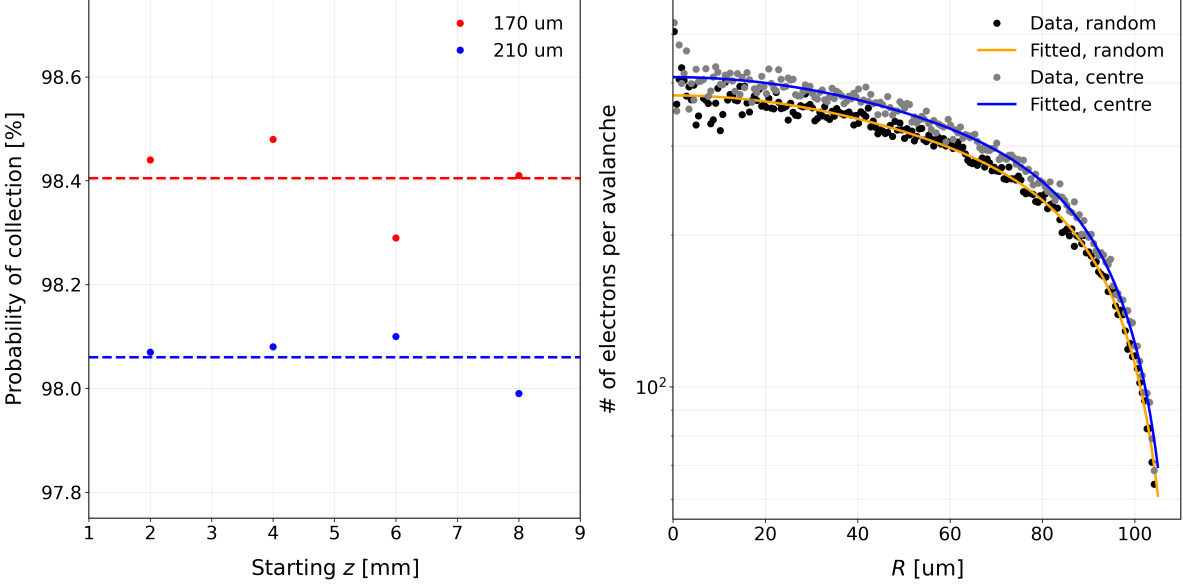


Figure 10: Left: Ratio of collection for GEMs with diameters 170 μm and 210 μm . Right: Distribution of electrons reaching the exit of a GEM hole, for electrons starting at a random position (orange) and at top-centre (blue).

meaning that it's impossible to build up statistics during the placement. In previous researches, simulations on GEM stacks was done by limiting the avalanche size to 10^3 – 10^4 electrons, giving only a qualitative discussion of position distribution. In this report, we present a way to estimate the complete avalanche, with potentially very low error in the gain.

5.1 Multi-stage simulation

We divide the full avalanche into several parts:

1. Drift into the first GEM in the drift region. Probability of collection Γ_d .
2. Avalanche in the GEM hole, stopping at the exit. Multiplication factor M .
3. Drift in the transport region to the top of the next GEM. Surviving ratio Γ_t .
4. Repeat 2. and 3. until electrons reach the exit of the last GEM.
5. Drift to the ITO in the induction region. Surviving ratio Γ_i .

The total gain for a stack of n GEMs can therefore be expressed as

$$G^{(n)} = \Gamma_d \Gamma_i (M)^n (\Gamma_t)^{n-1}, \quad (4)$$

with error

$$\frac{\sigma_G^{(n)}}{G^{(n)}} = \sqrt{\left(\frac{\sigma_{\Gamma_d}}{\Gamma_d}\right)^2 + \left(\frac{\sigma_{\Gamma_i}}{\Gamma_i}\right)^2 + \left(\frac{n\sigma_M}{M}\right)^2 + \left(\frac{(n-1)\sigma_{\Gamma_t}}{\Gamma_t}\right)^2}. \quad (5)$$

Without further assumptions and justifications, the method is likely to have a huge error, and would require a lot of labour work. However, we will show that in MIGDAL experiment's set-up, many effects that could result in errors (such as asymmetries) are completely washed out by electron avalanche.

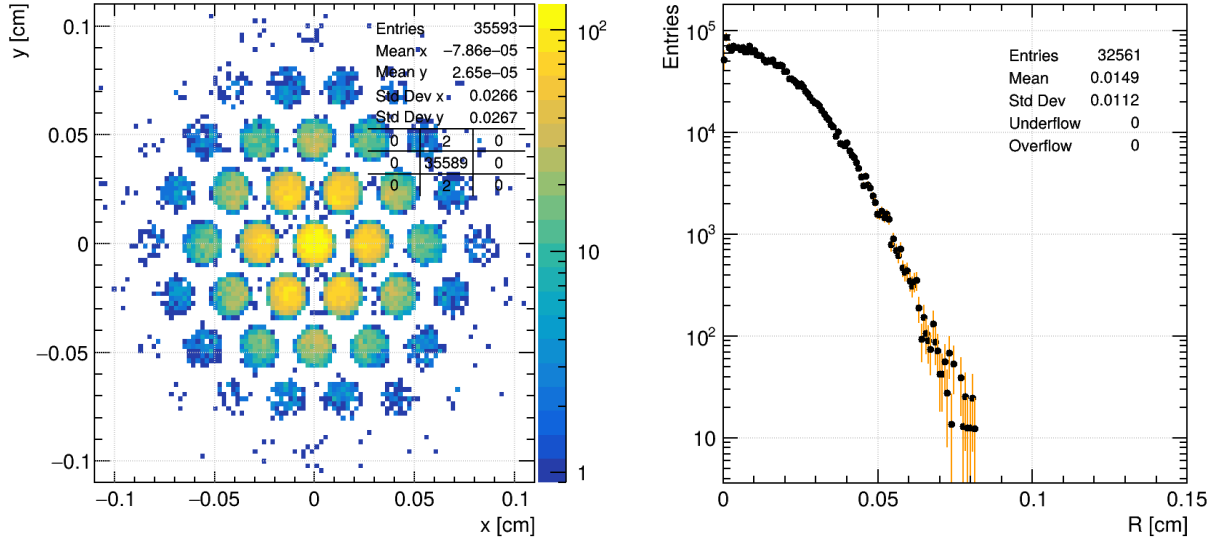


Figure 11: Left: Distribution of electrons survived to the top of the second GEM. Right: Distribution of electrons on the ITO, exiting from one GEM hole. Both plots are simulated using 10^5 electrons

As shown in Fig. 10 (left), the collection probability is not dependent on the starting z -coordinate in the drift region. However, GEM with 210 μm has a lower probability due to the "leakage" of electric field. This result confirms that GEM is a reliable detector for the Migdal electron, as every electron signal has $> 98\%$ probability to be amplified and detected.

For an avalanche in the GEM hole, the multiplication factor depends on the starting position of the electron. Electrons starting close to the glass wall has a higher probability to be lost within several mean free path's length, leading to a lower gain. Therefore, quantitative comparison between different starting point distributions is needed. As an example, we compare a neutral case — electrons starting at a random position — to an extreme case — electrons starting at top-centre of the GEM hole. The difference in M between them is 8.5 %, indicating that the gap to the actual situation should be much less.

A further comparison was made between electrons starting at a random position and electrons with $y > 0$ only. There was no difference in M (less than 0.5 %), and distribution of end points neither. From this, we could be confident to assume that any asymmetry in starting points will be "washed out" by avalanche, preserving the multiplication factor M . Simulated by 1×10^5 avalanches, the multiplication factor was determined to be 280.2 with 0.1 % error.

We then simulated the number of electrons entering different holes for the aligned and misaligned configurations. As asymmetry was washed out, we only need to consider the electrons exiting one hole, and apply it to other holes. Data is listed in Appendix A. Simulated using 3×10^6 electrons, the surviving factor Γ_t is 0.3587 for aligned GEMs and 0.3564 for misaligned.

Electron diffusion in the transport region gives a surviving factor $\Gamma_i = 0.3256$ and a distribution on the ITO with Full Width at Half Maximum (FWHM) 0.044 cm. A simple check on this result can be done using the transverse diffusion constant from Fig. 3. At 400 V cm^{-1} , FWHM for electrons starting at a single point should be

$$\text{FWHM} = 2\sqrt{2 \ln 2} \cdot \sigma = 2\sqrt{2 \ln 2} \cdot \sqrt{0.2 \text{ cm}} \times 0.0361 \text{ cm}^{1/2} = 0.038 \text{ cm}. \quad (6)$$

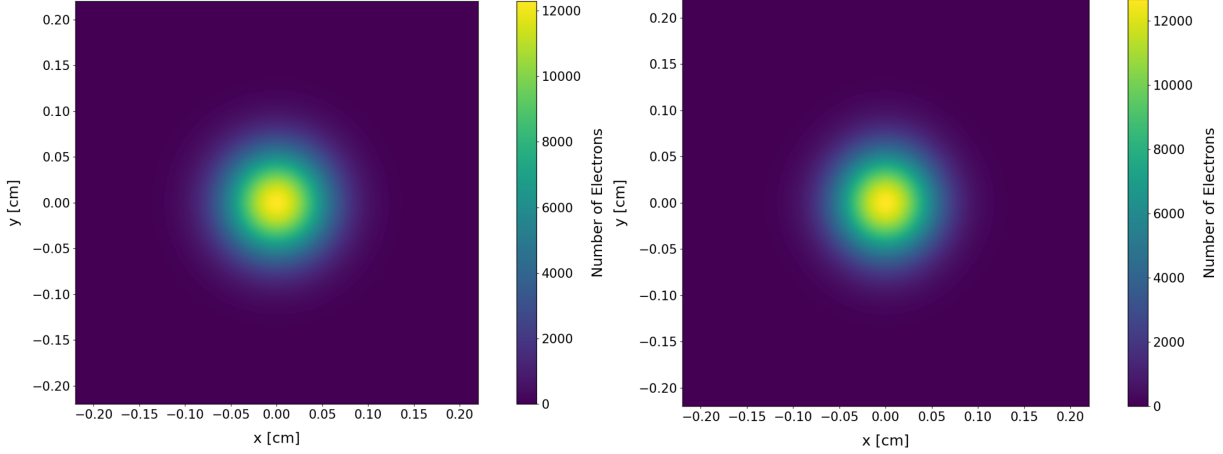


Figure 12: Electron distribution at the ITO plane for aligned GEMs (left) and misaligned (right). These two plots are using the same number of starting points, not necessarily normalised.

Considering the 0.021 cm diameter, our simulation match with the theoretical value well.

5.2 Gain and charge distribution on ITO

Combining the results above, the gain for three GEMs, 210 μm in diameter, 510 V across, is

$$G_{\text{aligned}}^{(3)} = 0.984 \times (280.15)^3 \times (0.3587)^2 \times 0.32561 = 9.066 \times 10^5 \quad (7)$$

for aligned GEMs and

$$G_{\text{misaligned}}^{(3)} = 0.984 \times (280.15)^3 \times (0.3564)^2 \times 0.32561 = 8.95 \times 10^5 \quad (8)$$

for misaligned. The combined statistical error is within 3 %, which can still be lower if we have more events.

From experiments [31], the gain for two GEMs with 210 μm was fitted to be

$$G_{\text{aligned}}^{(2)}(V) = 486 \cdot \exp(0.0548 \cdot V - 28), \quad G_{\text{aligned}}^{(2)}(510 \text{ V}) \simeq 461, \quad (9)$$

but our model would give a gain of 9020, which is significantly higher. This suggests the need of considering effects on electric field from ions and electrons themselves: For electrons in a huge electron/ion cloud, the applied electric field may be shielded, which decreases the gain significantly. Recently, a gain saturation model accounting for these effects were introduced by the CYGNO collaboration [32], a model similar in principle will be needed for the MIGDAL experiment.

As for position distributions within the ITO plane, the result for both aligned GEMs and misaligned GEMs are shown in Fig. 12. The Gaussian broadening in the induction region washed out all asymmetries, giving a roughly axial symmetric distribution of charge. The standard deviations in x and y are 413 μm for aligned GEMs and 397 μm for misaligned ones, which is not much different comparing to the 280 μm pitch. The similar distribution suggests that the choice between aligned and misaligned GEMs should be guided more by considerations of mechanical stability and charge accumulation behavior. Since aligned GEMs result in a slightly larger Γ_t , it could improve stability and robustness in gain.

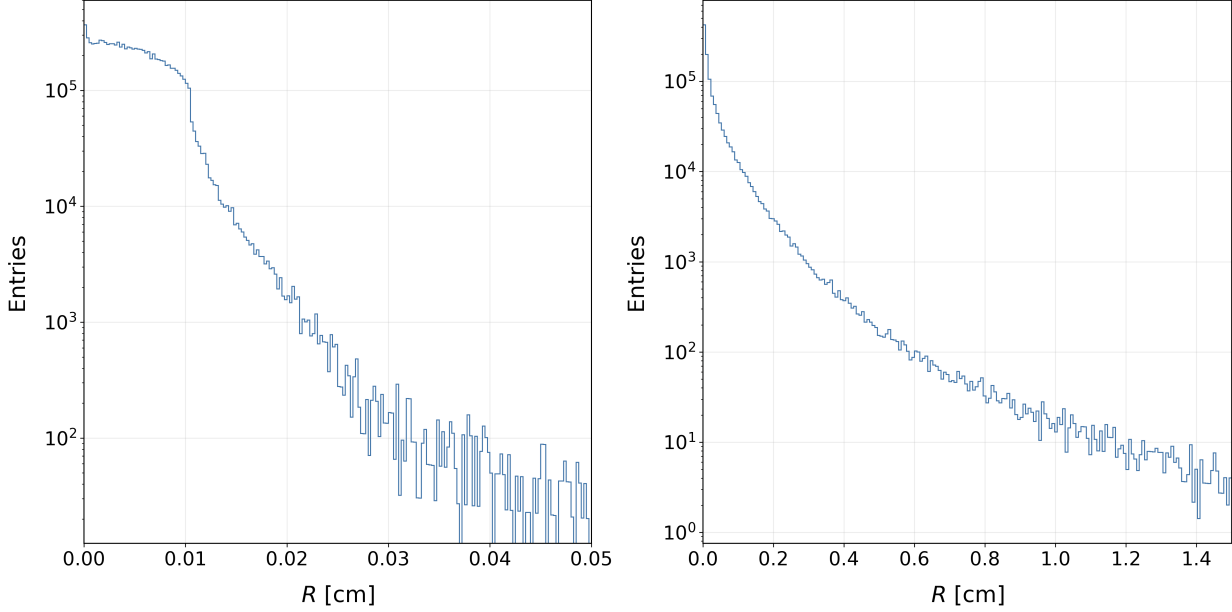


Figure 13: The distribution of radius on the BFG (left) and TSG (right) planes. Both distributions weighted by $1/r$.

5.3 Light collection map

The MIGDAL OTPC has a $8\text{ cm} \times 8\text{ cm} \times 3\text{ cm}$ fiducial volume, where electrical and optical signals can be efficiently captured. Trivially, due to geometrical limitations, the sensitivity of qCMOS to signals vary with positions. Since we have sufficient information about scintillation in GEMs, we can simulate this effect through similar procedures.

We will simulate three distributions before combining them to give the photon collection map. In 1000 avalanches in the central GEM hole in the first GEM, we would produce about 1.74×10^5 photons. Among them, 47900 will exit from the GEM hole. Distributions we want are:

- Positions of photons at the Bottom of the first GEM (BFG);
- Positions of photons at the Top of the Second GEM (TSG);
- Positions and directions of photons at the Top of the Third GEM (TTG);
- Positions and directions of photons at the ITO plane.

The Python code we used to tell if a photon is passing through a GEM is listed in Appendix B. In the code, the 2.79 rad lower limit of θ was set due to the geometrical limit of GEMs,

$$\theta \geq \frac{\pi}{2} + \arctan\left(\frac{574}{210}\right) \simeq 2.79\text{ rad.} \quad (10)$$

The BFG, TSG, and TTG distributions can be obtained directly, while the ITO distribution can be derived by applying an additional selection after calculating TTG. Compared with a full Monte Carlo simulation of electrons, these procedures are extremely efficient and can be completed within minutes.

The BFG and TSG distributions are shown in Fig. 13. Since the TSG distribution corresponds to photons on the ITO surface originating from a hole in the third GEM, we expect it to dominate

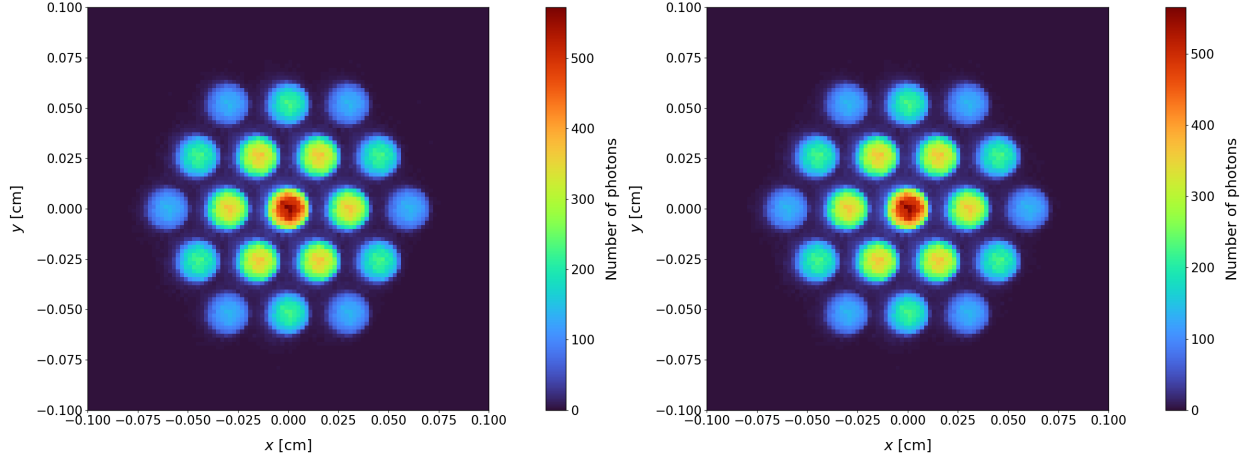


Figure 14: Number of photons reaching the plane of focus per avalanche, for aligned GEMs (left) and misaligned (right), with 100 bins in both directions.

the overall photon gain. Some photons produced at the bottom of the hole extend beyond the $10\text{ cm} \times 10\text{ cm}$ region, but this does not affect the readout, assuming the TPC walls are completely transparent.

The TTG distribution, shown in Fig. 15, is sensitive to the alignment of the GEMs. For aligned GEMs, a larger fraction of photons pass through, as the TSG distribution exhibits a sharp central peak. In contrast, for misaligned GEMs, fewer photons survive, since the geometry suppresses the central peak and blocks many photons from passing through the last GEM. Quantitatively, for aligned GEMs, 4325 photons pass the second GEM, and 1588 pass the third among the 47900 photons exiting from the GEM hole. The numbers for misaligned GEMs are 3887 and 1215 instead.

At $10^2\text{ }\mu\text{m}$ scale, it's crucial to examine diffraction effects. Suppose the VUV wavelength is 160 nm, the number of Fresnel half-wave zones is

$$N \simeq \frac{D^2}{4\lambda z} = \frac{(210\text{ }\mu\text{m})^2}{4 \cdot 160\text{ nm} \cdot 12\text{ cm}} = 0.57, \quad (11)$$

and for visible light, the number is even smaller, which means that: 1. It's not safe to treat light as particles; 2. Diffraction is dominated by the far-field Fraunhofer behaviour. For VUV, the Airy disk is about 224 μm in diameter, with first bright ring's intensity is 1.7 % that of the central peak. Although the holes in the last GEM act as an extended light source, so the diffraction patterns originating from the previous GEMs are effectively smeared out and become negligible on the plane of focus, additional checks are needed on the qCMOS plane, comparing the size of diffraction pattern and that of pixels.

Since there is an proportional relation between number of electrons and photons produced, we can generate photon distributions at the bottom of the last GEM. Using data from Appendix A, we computed a photon distribution at the bottom of the last GEM, normalised to one full avalanche, as shown in Fig. 14.

Similar to the distribution of electrons, distribution of photons vary only slightly with alignments. The structure of GEM is clearly seen in the photon distribution, suggesting that the optical readout is highly sensitive to the microscopic geometry of the holes. This sensitivity results in a non-uniform light yield across the plane of focus, with localized maxima at the projected hole positions and

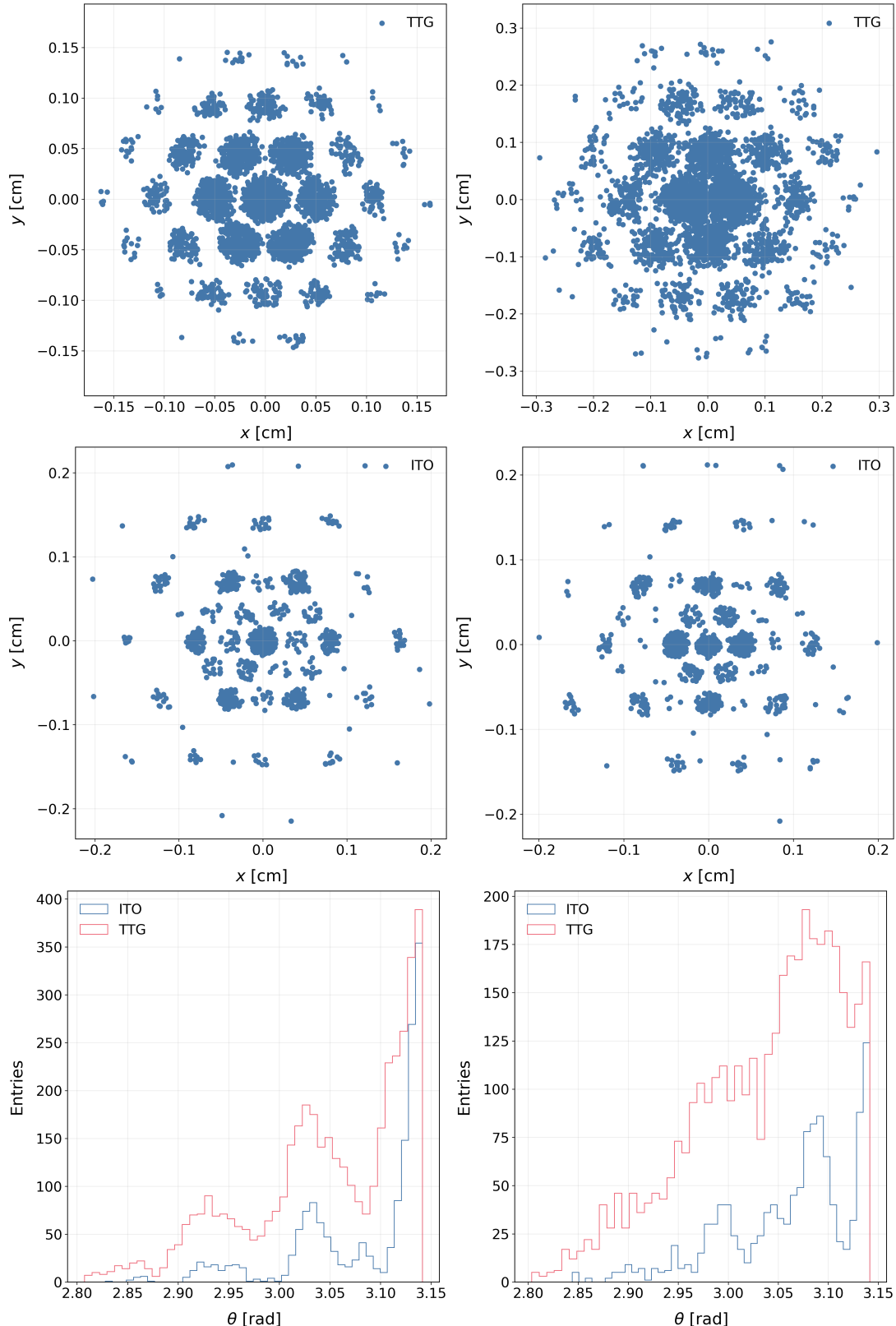


Figure 15: TTG (top) and ITO (middle) scatter plots and distribution of θ (bottom) for aligned GEMs (left) and misaligned (right).

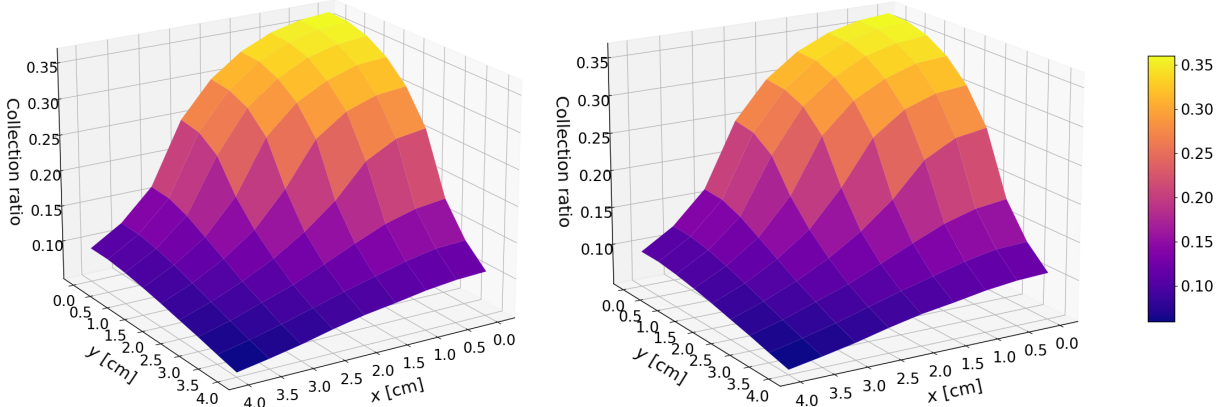


Figure 16: Map of photon collection ratio on the plane of focus in the range $x, y \in [0, 4]$, for aligned (left) and misaligned (right) GEMs. We assume ITO and the Kodial window are completely transparent.

reduced intensity between them. Consequently, the achievable spatial resolution is no longer limited by diffusion of charge alone, but also by the granularity of the optical response. Quantitative reconstruction studies show that the hole pitch and photon statistics set an effective lower bound on the position resolution, typically on the order of a fraction of the pitch when sufficient photon statistics are available [33].

Since photons are associated with the starting points of electrons, it is not safe to assume a uniform distribution at the bottom. In Fig. 14, we observe asymmetry within each hole, primarily due to the BFG distribution. However, the intensity resulting from this asymmetry (fewer than 100 photons per avalanche) is significantly lower than the intensity at the centers of the holes (up to 1000 photons per avalanche). Also, the electron startpoints in an event should be symmetric about the central axis, which gives an overall six-fold distribution. Therefore, our simulation remains valid and closely reflects the real case, with minimal deviation.

The ITO mesh is 1.1 mm thick, below it is a 63 mm gap, a 6 mm Kodial window, and a final 5 mm distance to the EHD-25085-C lens, respectively. The combined length from plane of focus to surface of the lens is 77.1 mm. Without the detailed structure within the lens, it is impossible to map photon collection on the qCMOS plane. But it is easy to calculate photon collection ratio at the camera, since the whole GEM is within the lens’s angle of view. Due to symmetry, we plot the collection ratio for an 9×9 array in the $x, y \in [0, 4]$ region, as shown in Fig. 16. Signals from the TPC edge-centre are ~ 3 times fainter compare to centre, and corners ~ 7 , which are roughly consistent with ^{55}Fe calibration results in Ref [31]. As shown in Fig. 17, misaligned GEMs behave better at the edges and worse at centre, which is consistent with the θ distribution in Fig. 15.

The photon collection map revealed a concentrated region of higher intensity at the center, with a smooth decrease toward the edges, reflecting the geometry of the setup and the acceptance of the optical system. These results confirm the feasibility of our approach to scintillation and photon propagation, providing insights into next-step simulations.

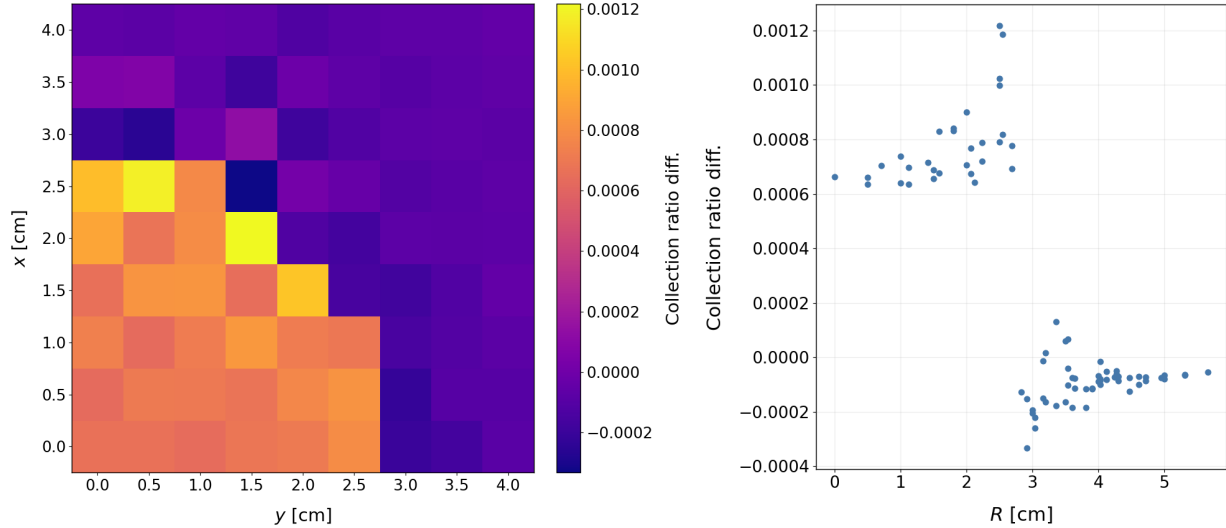


Figure 17: Left: Difference of collection ratio between aligned and misaligned GEMs. Aligned GEMs clearly perform better within a radius of $3 \sim 3.5$ cm, corresponding to the 2.79 rad threshold. Misaligned GEMs perform slightly better farther away. Right: Difference as a function of radius R , from the central axis of the detector.

6 Discussion and Conclusion

During the placement, detailed simulations for glass-GEMs with different geometry and properties were carried out. Built on previous work within the MIGDAL collaboration, we have introduced new concepts such as the necessity of field corrections, the multi-stage calculation of gain and 2D distribution, and the development of light collection maps.

Despite these advances, due to time constraints, there are limitations that we failed to break through and questions that this work failed to answer. We have already discussed some of them in the previous sections, such as the fundamental limitation of FEM, unknown scintillation mechanism of CF_4 -noble gas mixtures, and the effect of gain saturation. Additionally, operational data from the MIGDAL OTPC indicates a degradation in gain over time when using glass-GEMs [31]. While our simulations suggest this may result from charge accumulation on the glass walls or copper electrodes, we have not yet obtained quantitative evidence to support this hypothesis.

To address these open questions, future efforts should prioritise *theoretical understanding* on charge transport and scintillation properties in low-pressure gases, especially for CF_4 and noble gas mixtures. *Experimental validation* of the simulated effects — especially the long-term gain behavior and charge accumulation dynamics — is also needed to justify the gain from experiments quantitatively. In parallel, further refinement of the *simulation framework* is essential, involving hybrid methods that overcome FEM’s resolution bottlenecks, more accurately model microscopic charge transport, and take electric fields from electrons and ions into consideration. In addition, a detailed map of photon collection on the qCMOS plane can be done with knowledge about detailed structure of the lens, and investigation of diffraction effects will therefore be able to carry out. Hopefully, the integration of these theoretical, experimental, and computational advances into the broader context of MIGDAL’s detector optimisation strategy will be crucial for achieving improved energy and position resolutions.

Acknowledgements

I would like to express my sincere gratitude to my placement supervisor P. Majewski for his patience, guidance, and unwavering support throughout this project. I am also deeply thankful to H. Araujo, T. Marley, R. Bingham and T. Szwarcz for the many stimulating and insightful discussions, and to C. McCabe, D. Loomba, and F. Garcia for their valuable advice and directions.

I am grateful to all people at RAL for fostering a brilliant working environment and a culture of scientific excellence. Working at RAL has been both a privilege and a pleasure.

The placement was part of the 2025 PPD Summer Studentship at Rutherford Appleton Laboratory, supported by the Science and Technology Facilities Council.

References

- [1] J. Lewin and P. Smith, *Review of mathematics, numerical factors, and corrections for dark matter experiments based on elastic nuclear recoil*, *Astropart. Phys.* **6** (1996) 87.
- [2] XENON collaboration, *The XENONnT dark matter experiment*, *Eur. Phys. J. C* **84** (2024) .
- [3] D. Akerib et al., *The LUX-ZEPLIN (LZ) experiment*, *Nucl. Instrum. Meth. A* **953** (2020) 163047.
- [4] X. Cao et al., *PandaX: a liquid xenon dark matter experiment at CJPL*, *Sci. China Phys. Mech. Astron.* **57** (2014) 1476.
- [5] K.J. Kang et al., *Introduction to the CDEX experiment*, *Front. Phys.* **8** (2013) 412.
- [6] CDMS-II collaboration, *Dark Matter Search Results from the CDMS II Experiment*, *Science* **327** (2010) 1619.
- [7] M. Schumann, *Direct detection of WIMP dark matter: concepts and status*, *J. Phys. G: Nucl. Part. Phys.* **46** (2019) 103003.
- [8] L.D. Duffy and K.v. Bibber, *Axions as dark matter particles*, *New J. Phys.* **11** (2009) 105008.
- [9] W. Chao, J.-J. Feng and M. Jin, *Direct detections of the axionlike particle revisited*, *Phys. Rev. D* **109** (2024) 075044.
- [10] A.B. Migdal, *Ionization of atoms accompanying α - and β -decay*, *J. Phys. Acad. Sci. USSR* **4** (1941) 449.
- [11] M. Ibe et al., *Migdal Effect in Dark Matter Direct Detection Experiments*, *JHEP* **03** (2018) 194.
- [12] XENON collaboration, *Search for Light Dark Matter Interactions Enhanced by the Migdal Effect or Bremsstrahlung in XENON1T*, *Phys. Rev. Lett.* **123** (2019) 241803.
- [13] P. Cox et al., *Precise predictions and new insights for atomic ionization from the Migdal effect*, *Phys. Rev. D* **107** (2023) 035032.
- [14] D. Adams et al., *Measuring the Migdal effect in semiconductors for dark matter detection*, *Phys. Rev. D* **107** (2023) L041303.
- [15] N.F. Bell et al., *Observing the Migdal effect from nuclear recoils of neutral particles with liquid xenon and argon detectors*, *Phys. Rev. D* **105** (2022) 096015.
- [16] H. Araújo et al., *The MIGDAL experiment: Measuring a rare atomic process to aid the search for dark matter*, *Astropart. Phys.* **151** (2023) 102853.

- [17] F. Sauli, *GEM: A new concept for electron amplification in gas detectors*, *Nucl. Instrum. Meth. A* **386** (1997) 531.
- [18] P. Verwilligen, *GEM detectors for the CMS endcap muon system: status of three new detector stations*, *JINST* **18** (2023) C07006.
- [19] C. Shalem et al., *Advances in Thick GEM-like gaseous electron multipliers Part I: atmospheric pressure operation*, *Nucl. Instrum. Meth. A* **558** (2006) 475.
- [20] C. Shalem et al., *Advances in thick GEM-like gaseous electron multipliers Part II: Low-pressure operation*, *Nucl. Instrum. Meth. A* **558** (2006) 468.
- [21] A. Breskin et al., *A concise review on THGEM detectors*, *Nucl. Instrum. Meth. A* **598** (2009) 107.
- [22] Y. Mitsuya et al., *Development of large-area glass GEM*, *Nucl. Instrum. Meth. A* **795** (2015) 156.
- [23] J. Verbus et al., *Proposed low-energy absolute calibration of nuclear recoils in a dual-phase noble element TPC using D-D neutron scattering kinematics*, *Nucl. Instrum. Meth. A* **851** (2017) 68.
- [24] LUX-ZEPLIN collaboration, *First dark matter search results from the LUX-ZEPLIN (LZ) experiment*, *Phys. Rev. Lett.* **131** (2023) 041002.
- [25] XENON collaboration, *XENONnT WIMP search: Signal and background modeling and statistical inference*, *Phys. Rev. D* **111** (2025) 103040.
- [26] F.M. Brumbauer et al., *Primary and secondary scintillation of CF4-based mixtures in low-pressure gaseous detectors*, *Front. Detect. Sci. Tech.* **3** (2025) 1561739.
- [27] M. Fraga et al., *The GEM scintillation in He-CF4, Ar-CF4, Ar-TEA and Xe-TEA mixtures*, *Nucl. Instrum. Meth. A* **504** (2003) 88.
- [28] A. Kaboth et al., *A measurement of photon production in electron avalanches in CF4*, *Nucl. Instrum. Meth. A* **592** (2008) 63.
- [29] A. Bondar et al., *Light multi-GEM detector for high-resolution tracking systems*, *Nucl. Instrum. Meth. A* **556** (2006) 495.
- [30] F. Sauli, *The gas electron multiplier (GEM): Operating principles and applications*, *Nucl. Instrum. Meth. A* **805** (2016) 2.
- [31] T. Marley, *The MIGDAL experiment*, Ph.D. thesis, Imperial Coll., London, 2024. 10.25560/113387.
- [32] F.D. Amaro et al., *Modeling the light response of an optically readout GEM based TPC for the CYGNO experiment*, [2505.06362](#).
- [33] MIGDAL collaboration, *3D track reconstruction of low-energy electrons in the MIGDAL low pressure optical time projection chamber*, *JINST* **18** (2023) C07013.

A Distribution at the bottom of transport region

Table 2: Number of electrons entering each hole per 10^5 , for GEMs aligned. Location indicated using radius from the centre.

Radius [pitch]	Symmetry	# per hole	# total	Ratio
0	1	4911	4911	0.150
1	6	2859	17154	0.523
2	6	511	3066	0.094
3	6	27.2	163	0.005
4	6	0.7	4	0.000
$\sqrt{3}$	6	902.7	5416	0.165
$\sqrt{7}$	12	82.3	988	0.030
$\sqrt{13}$	12	3.3	40	0.001
$2\sqrt{3}$	6	4.7	28	0.001
Attachment	-	-	815	0.025
Out of range	-	-	< 10	0.000
Total 61 holes	-	-	32585	0.994

Table 3: Number of electrons entering each hole per 10^5 , for GEMs misaligned (the bottom layer shifted 1/2 pitch to the $+x$).

Radius [pitch]	Symmetry	# per hole	# total	Ratio
$1/2$	2	4512.5	9025	0.284
$\sqrt{3}/2$	2	3358	6716	0.212
$\sqrt{7}/2$	4	1872.75	7571	0.239
$3/2$	2	1376	2752	0.087
$\sqrt{13}/2$	4	769	3076	0.097
$5/2$	2	122.5	245	0.008
$3\sqrt{3}/2$	2	89.5	179	0.006
$\sqrt{19}/2$	4	155	620	0.020
$\sqrt{21}/2$	4	122.25	489	0.015
$\sqrt{31}/2$	4	57.25	229	0.007
$\sqrt{43}/2$	4	7.5	30	0.001
$\sqrt{37}/2$	4	18	72	0.002
$\sqrt{39}/2$	4	16.75	67	0.002
$7/2$	6	5	30	0.001
$\sqrt{57}/2$	4	0.75	3	0.000
Attachment	-	-	638	0.025
Out of range	-	-	< 10	0.000
Total 52 holes	-	-	31742	1.006

B Code for determining passage

```

# Define a function that judges if the photon is going to pass a circle centred at
# (xc,yc,zc) with radius rlim.
def through_circle(xc, yc, zc, rlim, x, y, z, theta, phi):
    dxy = (z - zc) * np.tan(np.pi - theta) # angle in radians
    dx = dxy * np.cos(phi)
    dy = dxy * np.sin(phi)
    dr = np.sqrt((x + dx - xc)**2 + (y + dy - yc)**2)
    if dr < rlim:
        return True
    else:
        return False

# Define a function that judges if the photon is going to pass a hole centred at (
# xc, yc, zc-(thick/2)) with radius rlim.
def through_hole(xc, yc, zc, rlim, x, y, z, theta, phi):
    thick = gap + 2 * copperThick
    if theta > 2.79:
        if through_circle(xc, yc, zc, rlim, x, y, z, theta, phi) and
           through_circle(xc, yc, zc - thick, rlim, x, y, z, theta, phi):
            return True
        else:
            return False
    else:
        return False

# Define a function that judges if the photon is going to pass the GEM.
def pass_GEM(positions, zc, rlim, x, y, z, theta, phi):
    x_list = [x for x, _ in positions]
    y_list = [y for _, y in positions]
    judge = 0
    for i in range(len(x_list)):
        if through_hole(x_list[i], y_list[i], zc, rlim, x, y, z, theta, phi):
            judge += 1
        else:
            pass
    if judge == 1:
        return True
    else:
        return False

# Define a function that counts the number of photons passing the GEM.
# Here x_pos, y_pos, etc. are array-like.
def pass_GEM_counter(positions, zc, rlim, x_pos, y_pos, z_pos, theta_pos, phi_pos):
    :
    count = 0
    indices = []
    for i in tqdm(range(len(x_pos))):
        if pass_GEM(positions, zc, rlim, x_pos[i], y_pos[i],
                    z_pos[i], theta_pos[i], phi_pos[i]):
            count += 1
            indices.append(i)
        else:
            pass
    return count, indices

```